Available online at www.sciencedirect.com
ScienceDirect
Journal of Sound and Vibration 301 (2007) 43–58
JOURNAL OF SOUND AND VIBRATION
www.elsevier.com/locate/jsvi

Dynamic analysis of a hyperbolic composite coupling

H. Ghoneim[a,*], D.J. Lawrie[b]

[a]*Rochester Institute of Technology, 76 Lomb Memorial Dr. Rochester, NY 14623, USA*
[b]*Lawrie Technology Inc., 227 Hathaway Street, Girard, PA 16417, USA*

Received 8 August 2005; received in revised form 1 August 2006; accepted 5 September 2006
Available online 15 December 2006

Abstract

A novel composite coupling is proposed: flexible hyperbolic composite coupling. In addition to enjoying the advantages of composite materials, the proposed coupling may provide some of the needed damping and can be readily integrated with a composite drive shaft into a single unit. A mathematical model of the coupling is developed based on the Timoshenko beam theory using the energy approach and the extended Lagrange's equations. The corresponding discrete equations of vibration are derived by using the Galerkin finite element method. The finite element analysis is programmed in MATLAB and applied to solve for the natural frequencies of the proposed coupling. The dynamic characteristics of the coupling (axial, torsional and bending natural frequencies) are studied in order to assess the merits and potential of the proposed coupling.

1. Introduction

Flexible couplings transmit torque, while accommodating certain amount of misalignment, from a prime mover to a driven unit of rotating equipment [1]. Stringent demands are placed on modern flexible couplings, including: higher torque capacity, higher operational speed (at or post-resonance), accommodation of more misalignments, less weight and cost. Taking advantages of the unique properties of composite materials (high specific stiffness and strength, engineering tailoring capability, and high fatigue strength and corrosion resistance), composite coupling have been introduced in an attempt to achieve the above-mentioned demands [2,3]. In this paper, a new flexible composite coupling: Hyperbolic Composite Coupling (HCC) is proposed. In addition to satisfying most of the demands imposed on modern coupling, the proposed coupling can provide some needed damping [4,5]. Moreover, the HCC can be readily manufactured with a composite drive shaft into a single integral-coupling-drive-shaft unit [6,7], which enjoys the attractive feature of low manufacturing and maintenance cost.

The mathematical model of the proposed coupling (HCC) is derived based on the Timoshenko beam assumptions, using the energy approach and the extended Lagrange's equations [8]. Then, the discrete standard equation of vibration ($[\mathbf{M}]\ddot{\underline{\mathbf{U}}}+[\mathbf{K}]\underline{\mathbf{U}}=\underline{\mathbf{0}}$) is derived by using a finite element method. The effect of two geometric parameters, for two types of fibrous composite materials, on the dynamic characteristics

*Corresponding author. Tel.: +1 585 475 2162; fax: +1 585 475 7710.
E-mail address: hngeme@rit.edu (H. Ghoneim).

0022-460X/$ - see front matter © 2006 Elsevier Ltd. All rights reserved.
doi:10.1016/j.jsv.2006.09.013

(the torsional, bending and axial natural frequencies) of the proposed coupling is studied. Based on this study, the potential of the proposed coupling is addressed.

2. Mathematical model

2.1. Constitutive equations and kinematics

The model of the flexible coupling is based on Timoshenko beam assumptions. In addition, the circular cross-sectional area is allowed to axially translate, rotate, and radially expand/contract. That is, the cross-sectional circular plane remains a circular plane, but not necessarily perpendicular to the axis of the coupling (first-order shear theory). Consequently, there are seven components of displacement that define the motion of a point on the cross-sectional area. Based on the inertial coordinates xyz shown in Fig. 1, where the x-axis coincides with the axis of the un-deformed coupling (dashed line), the four components of displacements that define the flexural motion of the cross-section of the coupling are: the transverse displacements, u_y and u_z, and the angular rotation about the y and z axes α and β, respectively. The other three displacements are: the axial displacement, u_x, angle of twist, ϕ, and the radial displacement, u_r. It is understood that, for the sake of illustration, the displacements in Fig. 1 are exaggerated.

In the current analysis, we assume that the through-thickness stress, σ_z and the tangential (hoop) stress, σ_θ, are negligible. We also assume that the radial strain component, ε_r, and the inter-laminar shear strain, $\gamma_{r\theta}$, are negligible. After two sets of coordinate transformation, from material coordinates to the meridian coordinates, $\bar{x}\theta\bar{z}$ (see Fig. 1), and then to the global inertial cylindrical coordinates [9] $x\theta r$, the constitutive equation for any ply in the laminate of the coupling becomes,

$$\begin{pmatrix} \sigma_x \\ \sigma_r \\ \tau_{r\theta} \\ \tau_{rx} \\ \tau_{x\theta} \end{pmatrix} = \begin{bmatrix} \tilde{Q}_{11} & \tilde{Q}_{15} & \tilde{Q}_{16} \\ \tilde{Q}_{31} & \tilde{Q}_{35} & \tilde{Q}_{36} \\ \tilde{Q}_{41} & \tilde{Q}_{45} & \tilde{Q}_{46} \\ \tilde{Q}_{51} & \tilde{Q}_{55} & \tilde{Q}_{56} \\ \tilde{Q}_{61} & \tilde{Q}_{65} & \tilde{Q}_{66} \end{bmatrix} \begin{pmatrix} \varepsilon_x \\ \gamma_{rx} \\ \gamma_{x\theta} \end{pmatrix}. \tag{1}$$

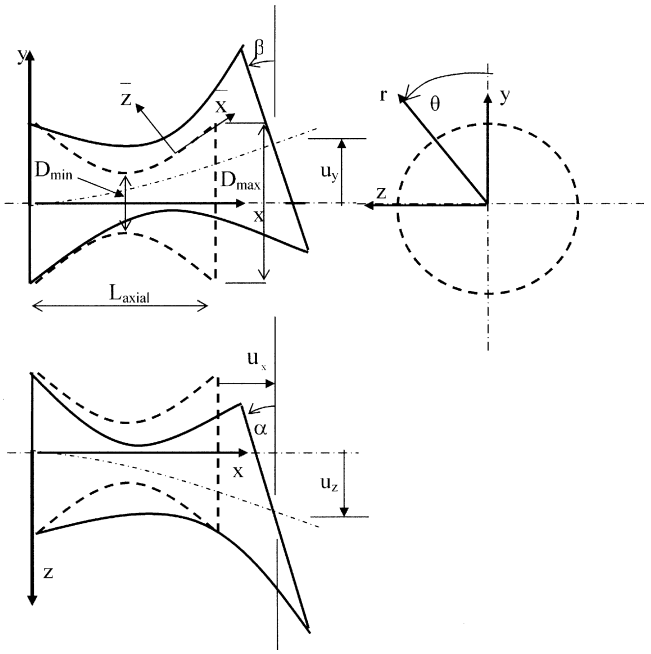

Fig. 1. Schematic of the different displacements of the hyperbolic coupling.

For a detailed derivation of the constitutive relation given in Eq. (1), see Appendix A. The strain components in Eq. (1) are given by

$$\begin{aligned}\varepsilon_x &= u_x' - (\beta' r + \beta r')\cos(\theta) + (\alpha' r + \alpha r')\sin(\theta),\\ \gamma_{x\theta} &= r\phi' + (u_z' + \alpha)\cos(\theta) - (u_y' - \beta)\sin(\theta),\\ \gamma_{rx} &= u_r' + (u_z' + \alpha)\sin(\theta) + (u_y' - \beta)\cos(\theta).\end{aligned} \tag{2}$$

The prime in Eq. (2) designates partial derivative with respect to x. Note that r is a function of the axial coordinate, that is, $r = c\sqrt{((x - L_{\text{axial}}/2)/d)^2 + 1}$, where c and d are the two geometric parameters defining the hyperbolic curve. The parameter c is the minimum radius, $R_{\min}$, of the hyperbola.

2.2. Energy expression

The potential energy of the coupling, U, derived using the assumptions introduced in Eq. (1), and where n is the number of layers (plies), is

$$U = \frac{1}{2}\int_0^L \sum_{i=1}^{n} \int_0^{2\pi r} \int_{ri}^{0} (\sigma_x \varepsilon_x + \tau_{rx}\gamma_{rx} + \tau_{x\theta}\gamma_{x\theta}) r \,\mathrm{d}r \,\mathrm{d}\theta \,\mathrm{d}x.$$

Substitute Eqs. (1) and (2) into this expression, then after some manipulation, the expression of the coupling's potential energy becomes

$$\begin{aligned}U = \frac{1}{2}\int_0^L \{&K_{MM}(\alpha'^2 + \beta'^2) + 2\overline{K}_{MM}(\beta\beta' + \alpha\alpha') + \widetilde{K}_{MM}(\beta^2 + \alpha^2)\\ &+ K_{VV}((u_z' + \alpha)^2 + (u_y' - \beta)^2) + 2K_{VB}(\alpha'(u_z' + \alpha) - \beta'(u_y' - \beta))\\ &+ 2K_{RB}(\alpha(u_z' + \alpha) - \beta(u_y' - \beta)) - 2K_{VA}(\beta'(u_z' + \alpha) + \alpha'(u_y' - \beta))\\ &- 2K_{RA}(\beta u_z' + \alpha u_y') + K_{PP}u_x'^2 + K_{TT}\phi'^2 + K_{RR}u_r'^2\\ &+ 2K_{PT}u_x'\phi' + 2K_{RT}u_r'\phi' + 2K_{PR}u_x'u_r'\} \,\mathrm{d}x.\end{aligned} \tag{3}$$

The kinetic energy of the coupling is

$$T = \frac{1}{2}\int_0^L \sum_{1}^{n} \int_0^{2\pi r} \int_{ri}^{0} \rho(v_x^2 + v_y^2 + v_z^2) r \,\mathrm{d}r \,\mathrm{d}\theta \,\mathrm{d}x.$$

The x, y and z components of the velocities of a generic point on the shaft are, respectively:

$$\begin{aligned}v_x &= \frac{\partial}{\partial t}\{u_x - r\cos\theta\sin\beta + r\sin\theta\sin\alpha\},\\ v_y &= \frac{\partial}{\partial t}\{u_y + r\cos\theta\cos\beta\},\\ v_z &= \frac{\partial}{\partial t}\{u_z + r\sin\theta\cos\alpha\}.\end{aligned} \tag{4}$$

Substituting Eqs. (4) into the kinetic energy expression, and after some manipulation, we obtain

$$\begin{aligned}T = \frac{1}{2}\int_0^L &m(\dot{u}_x^2 + \dot{u}_y^2 + \dot{u}_z^2 + \dot{u}_r^2) + I(2\dot{\phi}_s^2 + \dot{\alpha}_s + \dot{\beta}_s)\\ &+ 2I\dot{\theta}(\dot{\alpha}\sin\beta\cos\alpha - \dot{\beta}\sin\alpha\cos\beta) \,\mathrm{d}x,\end{aligned} \tag{5}$$

where, $\dot{\theta} = \Omega + \dot{\phi}$, with Ω as the spinning speed of the shaft, and is assumed constant. The dot over the letter signifies differentiation with respect to time, t. The expressions for the different stiffness, K, mass, m, and mass moment of inertia, I, in the potential and kinetic energy expressions can be found in the Appendix B. It is important to note that, because the radius and the fiber angle orientations vary with x, these stiffness and mass expressions are functions of the axial coordinate, x.

2.3. Mathematical model

The partial differential equation governing the dynamics of the HCC is derived from the extended Lagrange's equation [9]:

$$\frac{\partial \hat{L}}{\partial q_i} - \frac{\partial}{\partial_X}\left(\frac{\partial \hat{L}}{\partial q_i'}\right) - \frac{\partial}{\partial t}\left(\frac{\partial \hat{L}}{\partial \dot{q}_i}\right) = 0, \quad 0 < x < L,$$

and imposing the boundary conditions: $q_i = 0$, or $\partial \hat{L}/\partial q_i' = 0$ at both ends ($x = 0$, and $x = L$). In Lagrange's equation and the accompanied boundary conditions, $\hat{L} = \hat{T} - \hat{U}$, where $\hat{L}$ is the Lagrangian density, and $\hat{T}$ and $\hat{U}$ are the kinetic energy density and the potential energy density, respectively. The generic displacements $q_i, i = 1, 2, \ldots, 7$, stand for the seven displacement components, which completely define the motion of a point on the coupling. These displacements are $u_x, u_r, \phi, u_y, u_z, \beta$ and α. By substituting Eqs. (3) and (5) into Lagrange's equation, for each displacement component, we obtain, after some manipulation:

$$\begin{aligned}
&(K_{PP}u_x')' + (K_{PR}u_r')' + (K_{PT}\phi')' = m\ddot{u}_x,\\
&(K_{PR}u_x')' + (K_{RR}u_r')' + (K_{RT}\phi')' = m\ddot{u}_r,\\
&(K_{PT}u_x')' + (K_{RT}u_r')' + (K_{TT}\phi')' = \overline{I}\ddot{\phi} + \overline{I}(\ddot{\alpha}\beta - \beta\ddot{\alpha} + \alpha\beta(\dot{\beta}^2 - \dot{\alpha}^2)),
\end{aligned} \tag{6}$$

$$\begin{aligned}
&\{K_{VV}(u_y' - \beta) - K_{VB}\beta' - K_{RB}\beta - K_{VA}\alpha' - K_{RA}\alpha\}' = m\ddot{u}_y,\\
&\{K_{VV}(u_z' + \alpha) + K_{VB}\alpha' + K_{RB}\alpha - K_{VA}\beta' - K_{RA}\beta\}' = m\ddot{u}_z,
\end{aligned}$$

$$\begin{aligned}
&\{K_{MM}\beta' + \overline{K}_{MM}\beta - K_{VB}(u_y' - \beta) - K_{VA}(u_z' + \alpha)\}' - \overline{K}_{MM}\beta' - \widetilde{K}_{MM}\beta\\
&\quad - K_{VB}\beta' - K_{RB}(u_y' - 2\beta) - K_{VA}\alpha' + K_{RA}u_z' + K_{VV}(u_y' - \beta)\\
&\quad = I(\ddot{\beta} - 2\Omega\dot{\alpha} - 2\dot{\phi}\dot{\alpha} - \ddot{\phi}\alpha),
\end{aligned} \tag{7}$$

$$\begin{aligned}
&\{K_{MM}\alpha' + \overline{K}_{MM}\alpha + K_{VB}(u_z' + \alpha) - K_{VA}(u_y' - \beta)\}' - \overline{K}_{MM}\alpha' - \widetilde{K}_{MM}\alpha\\
&\quad - K_{VB}\alpha' - K_{RB}(u_z' + 2\alpha) + K_{VA}\beta' + K_{RA}u_y' - K_{VV}(u_z' + \alpha)\\
&\quad = I(\ddot{\alpha} + 2\Omega\dot{\beta} + 2\dot{\phi}\dot{\beta} + \ddot{\phi}\beta),
\end{aligned}$$

and the boundary conditions are given by

$$\begin{aligned}
&u_x = 0 \quad \text{or} \quad (K_{PP}u_x') + (K_{PR}u_r') + (K_{PT}\phi') = 0,\\
&u_r = 0 \quad \text{or} \quad (K_{PR}u_x') + (K_{RR}u_r') + (K_{RT}\phi') = 0,\\
&\phi = 0 \quad \text{or} \quad (K_{PT}u_x') + (K_{RT}u_r') + (K_{TT}\phi') = 0,\\
&u_y = 0 \quad \text{or} \quad \{K_{VV}(u_y' - \beta) - K_{VB}\beta' - K_{RB}\beta x - K_{VA}\alpha' - K_{RA}\alpha x\} = 0,\\
&u_z = 0 \quad \text{or} \quad \{K_{VV}(u_z' + \alpha) + K_{VB}\alpha' + K_{RB}\alpha x - K_{VA}\beta' - K_{RA}\beta x\} = 0,\\
&\beta = 0 \quad \text{or} \quad \{K_{MM}\beta' + \overline{K}_{MM}\beta - K_{VB}(u_y' - \beta) - K_{VA}(u_z' + \alpha)\} = 0,\\
&\alpha = 0 \quad \text{or} \quad \{K_{MM}\alpha' + \overline{K}_{MM}\alpha + K_{VB}(u_z' + \alpha) - K_{VA}(u_y' - \beta)\} = 0.
\end{aligned} \tag{8}$$

Eqs. (6) and (7) are coupled partial differential equations that represent the axial, radial, torsional and flexural vibration of the proposed coupling. The axial, radial and torsional Eqs. (6) are completely coupled. The transverse and rotational motions, of the flexural vibration of the coupling, Eq. (7), are also completely coupled. Both the axial–radial–torsional vibration, Eq. (6), and the flexural vibration, Eq. (7), are coupled through nonlinear inertial terms. In the current analysis, these nonlinear inertial terms are ignored, which uncouples the axial–radial–torsional vibration and the flexural vibration. The coupled equations of motion, Eqs. (6) and (7), subject to the boundary conditions, Eq. (8), constitute the mathematical model of the proposed coupling. These equations are solved to obtain the fundamental axial, torsional and bending natural frequencies of the coupling by using Galerkin finite element method coded in MATLAB. The solution is

obtained for the special case where the nonlinear inertial terms and the spin, Ω, are ignored. The effects of the nonlinear terms and the spin will be studied in a future work.

2.4. Discrete equation of motion

Over each element the generalized displacements are expanded in terms of the shape functions and the nodal displacements:

$$\begin{aligned}
&u_x(x,t)=\sum_{nn} N_i(x)U_{x_i}(t), \quad u_r(x,t)=\sum_{nn} N_i(x)U_{r_i}(t),\\
&\phi(x,t)=\sum_{nn} N_i(x)\Phi_i(t),\\
&u_y(x,t)=\sum_{nn} \xi_i(x)U_{y_i}(t), \quad u_z(x,t)=\sum_{nn} \xi_i(x)U_{z_i}(t),\\
&\alpha(x,t)=\sum_{nn} \eta_i(x)A_i(t), \quad \beta(x,t)=\sum_{nn} \eta_i(x)B_i(t),
\end{aligned} \tag{9}$$

where $U_{x_i}, U_{r_i}, \Phi_i, U_{y_i}, U_{z_i}, A_i$, and B_i are the nodal displacements, and $N_i(x), \xi_i(x)$, and $\eta_i(x)$ are the shape functions. For the current analysis, the cubic Hermite shape functions [10] with $nn=4$ are adopted for all three shape functions.

The element equation,

$$\mathbf{M^e}\ddot{\mathbf{U}}^{\mathbf{e}}+\mathbf{K^e}\mathbf{U^e}=\mathbf{b^e},$$

where $\mathbf{M^e}$ and $\mathbf{K^e}$ are the element mass and stiffness matrix, respectively, and $\mathbf{b^e}$ is the boundary force vector, is derived following the Galerkin finite element method [10]. First, the approximate, expanded solutions of the seven generalized displacements, Eq. (9), are substituted into the equations of motion, Eqs. (6) and (7), rendering the residuals $R_j(R_{ux}, R_{ur}, R_{\varphi}, R_{uy}, R_{uz}, R_{\beta}$ and $R_{\alpha})$. Second, the integrals of the weighted-residual are enforced to vanish over the element, that is; $\int_0^h w_j(x)R_j\,\mathrm{d}x=0$, where $w_j(x)$ are the weighting functions. In the Galerkin finite element method these weighting functions are taken as the shape functions: $N(x)$ for R_{ux}, R_{ur}, and R_{φ}; $\xi(x)$ for R_{uy} and R_{uz}; and $\eta(x)$ for R_{β} and R_{α}. Finally, the weighted-residual equations are integrated by part to yield the corresponding weak forms, which upon rearrangement and taking the appropriate boundary conditions into consideration result in the element equation $\mathbf{M^e}\ddot{\mathbf{U}}^{\mathbf{e}}+\mathbf{K^e}\mathbf{U^e}=\mathbf{b^e}$, where

$$\mathbf{M^e}=\begin{bmatrix}
\mathbf{Mx} & \mathbf{0} & \mathbf{0} & \mathbf{0} & \mathbf{0} & \mathbf{0} & \mathbf{0}\\
\mathbf{0} & \mathbf{Mr} & \mathbf{0} & \mathbf{0} & \mathbf{0} & \mathbf{0} & \mathbf{0}\\
\mathbf{0} & \mathbf{0} & \mathbf{Mp} & \mathbf{0} & \mathbf{0} & \mathbf{0} & \mathbf{0}\\
\mathbf{0} & \mathbf{0} & \mathbf{0} & \mathbf{MM} & \mathbf{0} & \mathbf{0} & \mathbf{0}\\
\mathbf{0} & \mathbf{0} & \mathbf{0} & \mathbf{0} & \mathbf{MM} & \mathbf{0} & \mathbf{0}\\
\mathbf{0} & \mathbf{0} & \mathbf{0} & \mathbf{0} & \mathbf{0} & \mathbf{JJ} & \mathbf{0}\\
\mathbf{0} & \mathbf{0} & \mathbf{0} & \mathbf{0} & \mathbf{0} & \mathbf{0} & \mathbf{JJ}
\end{bmatrix},$$

and

$$\mathbf{K}^{\mathrm{e}}=\begin{bmatrix}
\mathbf{K_{xx}} & \mathbf{K_{xr}} & \mathbf{K_{xp}} & \mathbf{0} & \mathbf{0} & \mathbf{0} & \mathbf{0}\\
\mathbf{K_{xr}} & \mathbf{K_{rr}} & \mathbf{K_{rp}} & \mathbf{0} & \mathbf{0} & \mathbf{0} & \mathbf{0}\\
\mathbf{K_{xp}} & \mathbf{K_{xr}} & \mathbf{K_{pp}} & \mathbf{0} & \mathbf{0} & \mathbf{0} & \mathbf{0}\\
\mathbf{0} & \mathbf{0} & \mathbf{0} & +\mathbf{K_{uu}} & \mathbf{0} & -\mathbf{K_{ub}} & -\mathbf{K_{ua}}\\
\mathbf{0} & \mathbf{0} & \mathbf{0} & \mathbf{0} & +\mathbf{K_{uu}} & -\mathbf{K_{ua}} & +\mathbf{K_{ub}}\\
\mathbf{0} & \mathbf{0} & \mathbf{0} & -\mathbf{K_{bu}} & -\mathbf{K_{au}} & +\mathbf{K_{bb}} & -\mathbf{K_{ba}}\\
\mathbf{0} & \mathbf{0} & \mathbf{0} & -\mathbf{K_{aua}} & +\mathbf{K_{bu}} & +\mathbf{K_{ba}} & +\mathbf{K_{bb}}
\end{bmatrix}.$$

Each element of the block matrices $\mathbf{M}^e$, and $\mathbf{K}^e$ is a 4×4 matrix, and the expressions of these elements are given in Appendix B. Notice that, because of the negligence of the nonlinear inertial terms, the axial–radial–torsional (the top-left 3×3 block matrices) and the flexural (the bottom-right 4×4 block matrices) of the stiffness matrix $[K]^e$ are uncoupled. It is understood that the discrete equation of motion is recovered upon the assembly of all element equations.

3. Results and discussion

The finite element program developed for the axial–radial–torsional and flexural vibration of the composite coupling is applied to determine the fundamental axial, torsional and bending frequencies of specific couplings. Two generic fibrous composite materials are examined: carbon/epoxy and carbon/polyurethane. A $[\pm\theta_f(x)]$ laminate is considered for the coupling, where θ_f is the fiber angle orientation. It is a function of the axial coordinates x, since the fibers are laid down along the geodesic lines of the hyperboloid (Appendix C). The material properties and dimensions of the two coupling under investigation are given in Table 1. Because this coupling has been produced in the USA, the unit of length adopted throughout the paper is in an inch ($1\,\text{in} = 2.54\,\text{cm}$).

In the flexible composite coupling examples, the carbon fiber and the epoxy are assumed to be elastic, and the polyurethane (matrix material) is assumed to be viscoelastic with a complex shear modulus. Because of the large difference in the moduli of the carbon and polyurethane, it is reasonable to assume that only E_2 and G_{23} will demonstrate substantial viscoelastic behavior [11]. Consequently, both E_2 and G_{23} are assumed complex; that is: $E_2 = E_2'(1 + \eta i)$ and $G_{23} = G_{23}'(1 + \eta i)$. The values of E_2' and G_{23}' are given in Table 1, and a quoted value of the material damping factor, $\eta = 0.1$, is adopted [12].

3.1. Carbon/epoxy results

The fundamental axial, torsional and bending natural frequencies as a function of $R_{\min}$, for the specific case of $L_{\text{axial}} = 6\,\text{in}$, are displayed in Fig. 2. Also, shown in Fig. 2 are the corresponding finite element results from ANSYS. For the ANSYS results, a mesh of 16×16 (16 circumferential element $\times 16$ axial element) shell99 composite elements was adopted. All the results shown are for the cantilevered case, that is, using fixed–free boundary conditions. The results of the developed finite element program are in close agreement with the ANSYS results. Initially a stiffening effect is observed in the torsional and bending modes as $R_{\min}$ is decreased from the cylindrical shape ($R_{\min} = R_{\max} = 3\,\text{inches}$); this is followed by a monotonic softening effect as $R_{\min}$ is further decreased. The axial stiffness (natural frequency) continues to drop as $R_{\min}$ decreases. The jump phenomenon observed in the axial natural frequency is attributed to the eigenvalue curve veering phenomenon [13,14], as explained in Appendix D.

The effect of the coupling length (L_{axial}) and $R_{\min}$ on the fundamental torsional, bending and axial natural frequencies of the coupling is displayed, in Fig. 3. In general, the natural frequencies of all three modes increase as the coupling is shortened (Figs. 3a–c), and as $R_{\min}$ increases (Figs. 3d–f). At small $R_{\min}$, however,

Table 1
Geometric and material properties of the composite coupling

Material properties	Carbon/epoxy	Carbon/polyurethene
Maximum radius, cm (in)	7.62 (3)	7.62 (3)
Thickness, mm (in)	0.0508 (0.02)	0.0508 (0.02)
E_1, GPa (Msi)	132 (19.2)	131 (19)
E_2, GPa (Msi)	10.8 (1.56)	0.21 (0.03)
G_{12}, GPa (Msi)	5.56 (0.82)	0.083 (0.012)
G_{23}, GPa (Msi)	3.38 (0.49)	0.028 (0.004)
v_{12} and v_{23}	0.24 and 0.59	0.4 and 0.8
ρ, kg/m^3 (lb s^2/in^4)	1540 (1.44×10^{-4})	1475 (1.37×10^{-4})

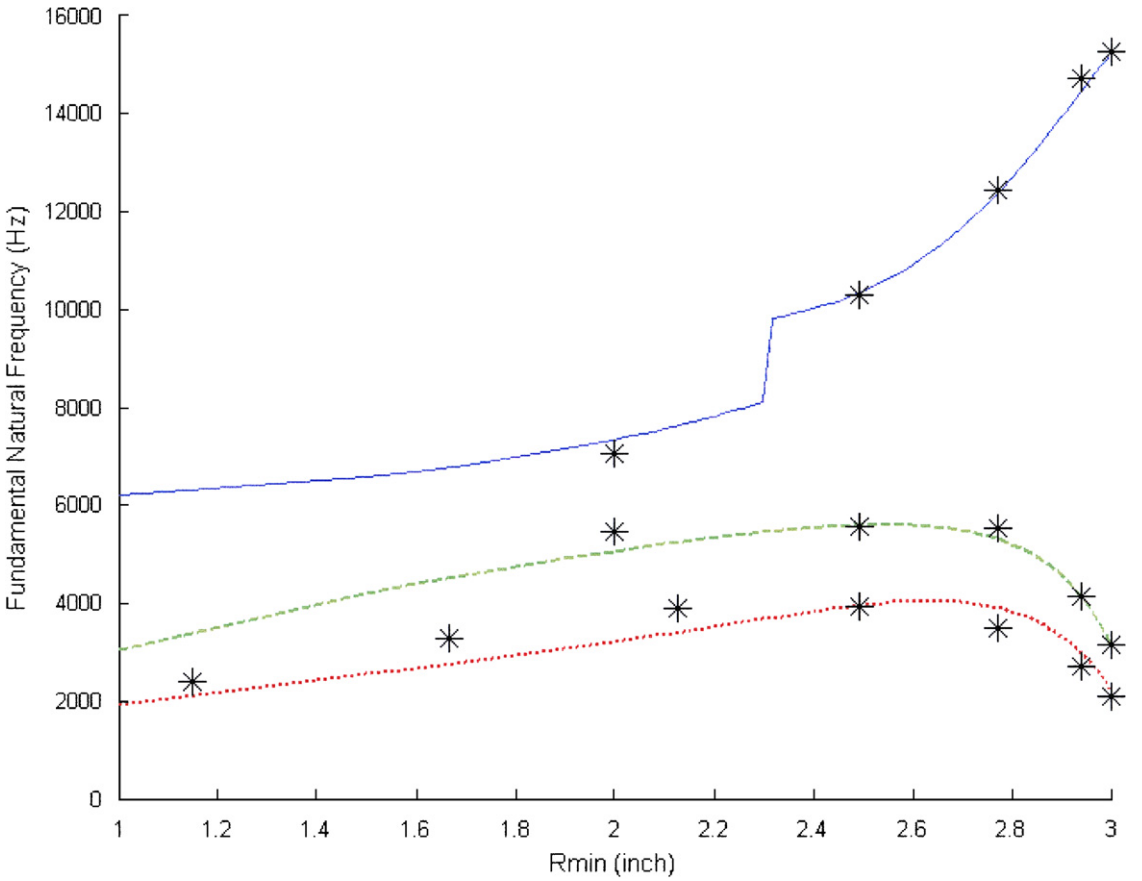

Fig. 2. The variation of the fundamental natural frequencies with R_{min}: ——— axial, ----- torsional, ... bending, $*$ ANSYS ($R_{max} = 3\,in = 7.62\,cm$, and $L_{axial} = 6\,in = 15.24\,cm$).

the bending natural frequency exhibits an optimum value of L_{axial} at which a maximum bending frequency occurs, and below which the bending frequency continues to drop as the coupling gets shorter (Fig. 3b). A peak torsional (Fig. 3d) as well as bending (Fig. 3e) natural frequency is also depicted as R_{min} approaches R_{max}; that is, as the hyperbolic coupling converges to a cylinder.

3.2. Carbon/polyurethane results

The fundamental axial and bending natural frequencies as a function of R_{min}, for the specific case of $L_{axial} = 6\,in$, are displayed in Fig. 4. Also, shown in the figure are the corresponding results from ANSYS. For the ANSYS results, a mesh of 16×8 (16 circumferential element $\times$ 8 axial element) shell99 composite elements were adopted. All results shown are for the cantilevered case, that is, fixed-free boundary conditions. As R_{min} approaches R_{max} and the hyperbolic coupling converges to a cylinder, the flexural natural frequency predictions exhibit a sharp peak, which is not observed in the ANSYS results (Fig. 4b). Aside form this discrepancy, the ANSYS and the developed finite element results show "reasonable" agreement. In practice, in order to achieve the needed axial and flexural flexibility of the coupling, R_{min} is confined to values less than 2 in—for $R_{max} = 3\,in$. For this practical range of R_{min} ($R_{min} < 2\,in$) there is reasonable agreement between the results of ANSYS and the developed program (Fig. 4), and consequently the following parametric study is confined to this range of R_{min}.

The effect of the coupling length (L_{axial}) and R_{min} on the fundamental torsional, bending and axial natural frequencies and the corresponding damping factors of the coupling are demonstrated in Fig. 5. Observe that

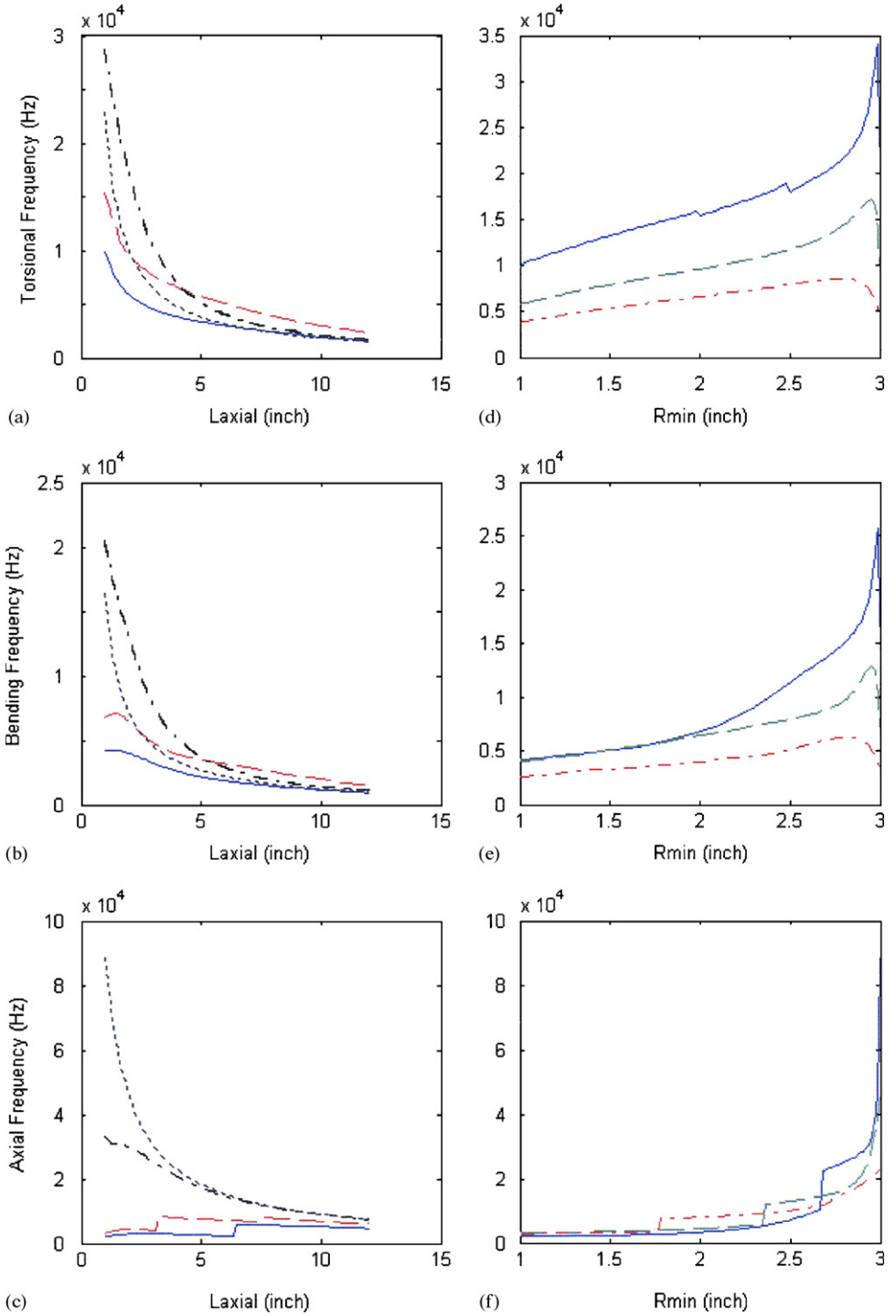

Fig. 3. The effect of the L_{axial} and R_{min} on the fundamental natural frequencies: (a) L_{axial} on the torsional, (b) L_{axial} on the bending, (c) L_{axial} on the axial, —— $R_{min} = 1$ in, —— $R_{min} = 2$ in, —·—·— $R_{min} = 2.95$ in, - - - - $R_{min} = 3$ in, (d) R_{min} on the torsional, (e) R_{min} on the bending, (f) R_{min} on the axial. —— $L_{axial} = 1$ in, —— $L_{axial} = 2$ in, —·—·— $L_{axial} = 4$ in.

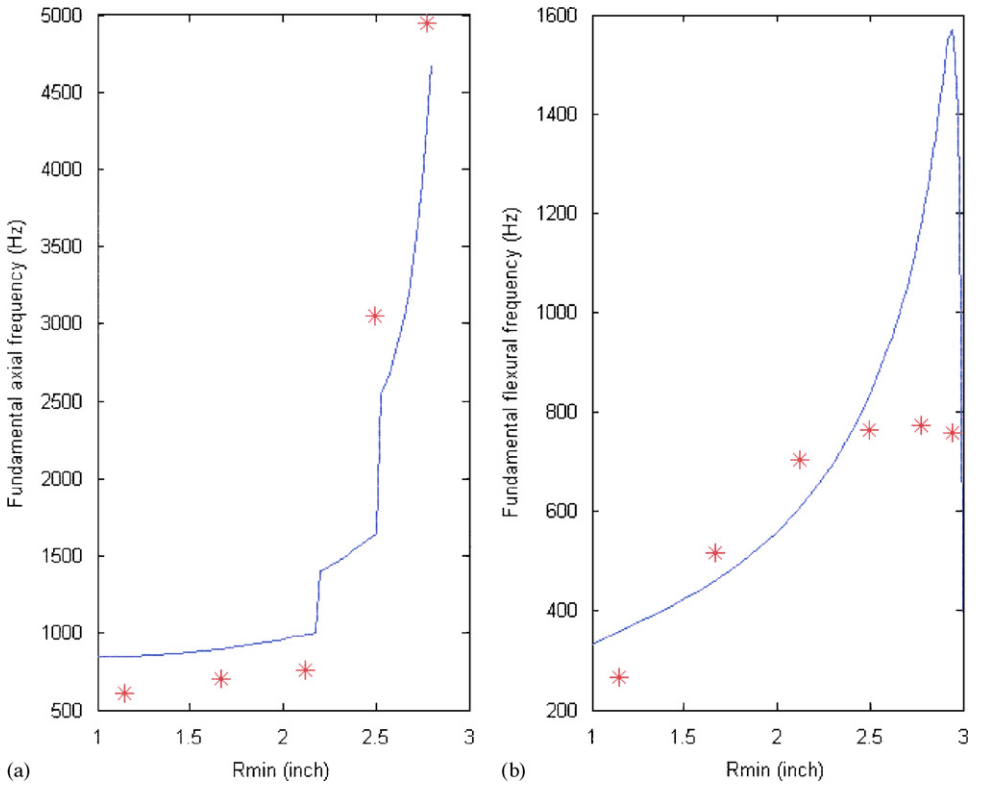

Fig. 4. The variation of the fundamental axial and bending natural frequencies with R_{min}: (a) axial, (b) bending. ——— finite element, ∗ ANSYS.

R_{min} is confined to values less than 2 in. In general, the fundamental natural frequencies of all three modes increase as R_{min} increases (Figs. 5a–c). In the range of L_{axial} and R_{min} covered in this paper, as L_{axial} decreases, the torsional natural frequency increases (Fig. 5c), and the bending and axial natural frequencies increase then decrease indicating the existence of optimum lengths, L_{axial}, at which a maximum bending frequency and a maximum axial frequency occur (Figs. 5a,b). This phenomenon is also depicted for carbon/epoxy hyperbolic couplings (Fig. 3). The effect of R_{min} and L_{axial} on the damping factor (Figs. 5d–f), in general, is insignificant. It should be pointed out that for an effective design of a flexible coupling, a high torsional natural frequency (stiff in torsion) and a relatively low bending and axial frequencies (flexible in bending and axial deflection) are required. The results in this preliminary analysis indicate that for $R_{min} = 1$ in and $L_{axial} = 1$ in a high torsional natural frequency (Fig. 5c) and low bending and axial frequencies (Figs. 5a,b) can be achieved. The jump phenomenon experienced with the axial and torsional frequencies and the corresponding discontinuity in the damping factors is attributed to the coupling among the different modes (curve veering) as explained earlier.

4. Conclusion

A novel coupling is presented: a flexible hyperbolic composite coupling. In addition to enjoying the advantages of composite materials, the proposed coupling can be readily integrated with composite drive shaft into a single unit. Moreover, the proposed coupling may provide some of the needed damping. The relevant dynamic characteristics of the coupling are investigated in this work. Specifically, the effect of two geometric parameters (minimum radius and axial length) and two carbon fibrous composite materials (carbon/epoxy and carbon/polyurethane) on the axial, torsional and bending natural frequency of the coupling is studied. These

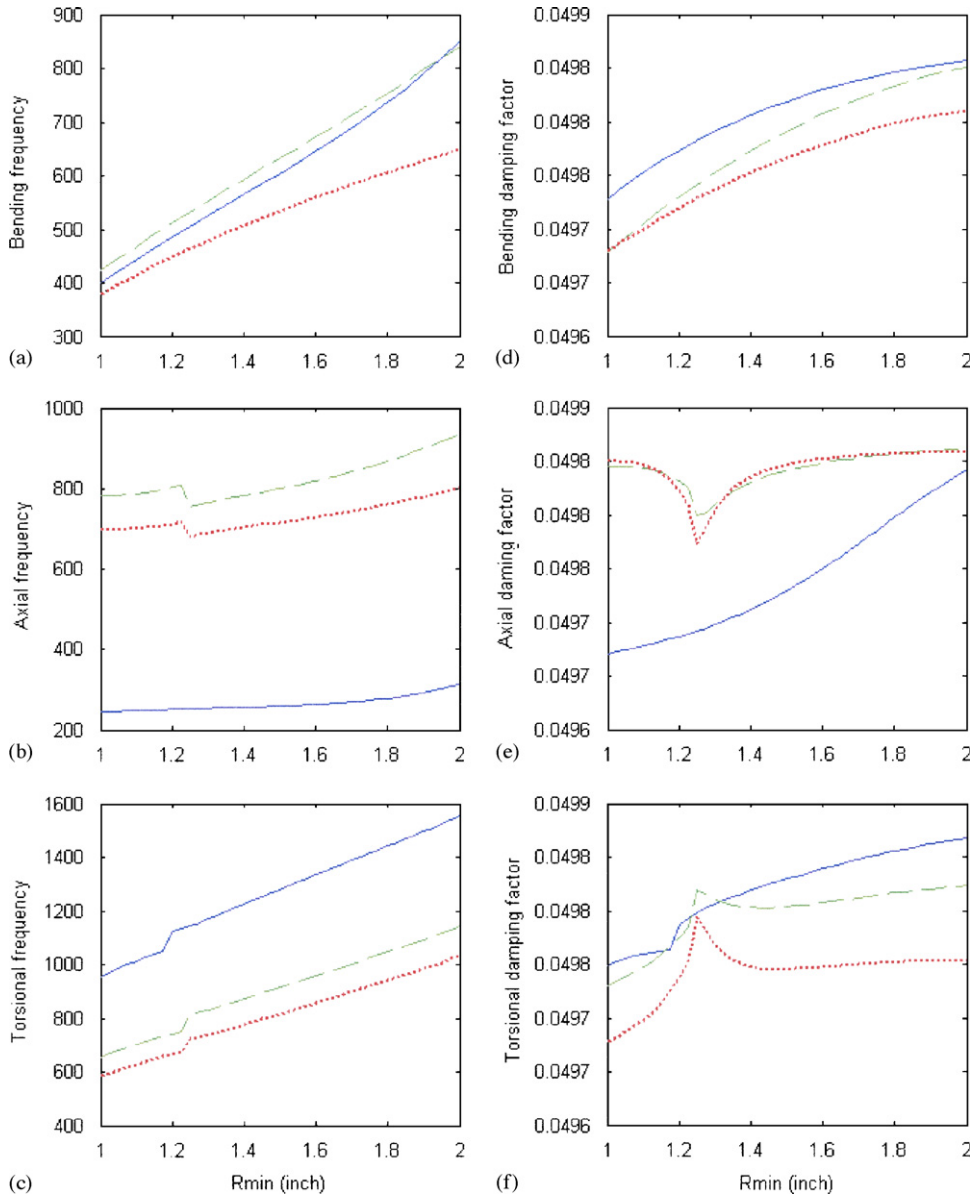

Fig. 5. The effect of L_{axial} and R_{min} on the fundamental natural frequencies and the corresponding damping factors: (a) bending natural frequency, (b) axial frequency, (c) torsional frequency, (d) bending damping factor, (e) axial damping factor, (f) torsional damping factor. ——— $L_{axial} = 1$ in, - - - - - $L_{axial} = 2$ in, ... $L_{axial} = 3$ in.

three characteristics are relevant because an effective coupling is one that acquires a high torsional natural frequency (stiff in torsion) and relatively low bending and axial frequencies (flexible in bending and axial deflection). A mathematical model of the coupling is developed based on the Timoshenko beam theory using the energy approach. The corresponding discrete equation of vibration are derived by using the Galerkin finite element method. The finite element analysis is programed in MATLAB and applied to solve for the natural frequencies of the proposed coupling. The results, in general, indicate that for the proposed coupling to be viable, small R_{min} and axial length, L_{axial}, are needed. Implementation of the proposed coupling with a composite shaft into an integrated driveshaft-coupling unit, and a study of the dynamic and strength characteristics of the integrated unit, is the subject of future work.

Appendix A. Constitutive equation in global coordinates

The constitutive equation of the fibrous composite material in the meridian coordinates of the surface of the hyperbola can be expressed as

$$\begin{pmatrix} \sigma_x \\ \sigma_\theta \\ \sigma_z \\ \tau_{yz} \\ \tau_{xz} \\ \tau_{xy} \end{pmatrix} = \begin{bmatrix} \overline{Q}_{11} & \overline{Q}_{12} & \overline{Q}_{13} & 0 & 0 & \overline{Q}_{16} \\ \overline{Q}_{12} & \overline{Q}_{22} & \overline{Q}_{23} & 0 & 0 & \overline{Q}_{26} \\ \overline{Q}_{13} & \overline{Q}_{23} & \overline{Q}_{33} & 0 & 0 & \overline{Q}_{36} \\ 0 & 0 & 0 & \overline{Q}_{44} & \overline{Q}_{45} & 0 \\ 0 & 0 & 0 & \overline{Q}_{45} & \overline{Q}_{55} & 0 \\ \overline{Q}_{16} & \overline{Q}_{26} & \overline{Q}_{36} & 0 & 0 & \overline{Q}_{66} \end{bmatrix} \begin{pmatrix} \varepsilon_{\overline{x}} \\ \varepsilon_\theta \\ \varepsilon_{\overline{z}} \\ \gamma_{\overline{yz}} \\ \gamma_{\overline{xz}} \\ \gamma_{\overline{xy}} \end{pmatrix}. \tag{A.1}$$

Taking into consideration the assumption that both the through-thickness meridian stress, $\sigma_{\overline{z}}$, and the hoop stress, σ_θ, are negligible, the corresponding strain components $\varepsilon_{\overline{z}}$ and ε_θ can be eliminated from Eq. (A.1), giving:

$$\begin{pmatrix} \sigma_x \\ \tau_{\theta z} \\ \tau_{xz} \\ \tau_{x\theta} \end{pmatrix} = \begin{bmatrix} \overline{\overline{Q}}_{11} & 0 & 0 & \overline{\overline{Q}}_{16} \\ 0 & \overline{Q}_{44} & \overline{Q}_{45} & 0 \\ 0 & \overline{Q}_{45} & \overline{Q}_{55} & 0 \\ \overline{\overline{Q}}_{16} & 0 & 0 & \overline{\overline{Q}}_{66} \end{bmatrix} \begin{pmatrix} \varepsilon_{\overline{x}} \\ \gamma_{\overline{\theta z}} \\ \gamma_{\overline{xz}} \\ \gamma_{\overline{x\theta}} \end{pmatrix}. \tag{A.2}$$

where

$$\begin{bmatrix} \overline{\overline{Q}}_{11} & \overline{\overline{Q}}_{16} \\ \overline{\overline{Q}}_{16} & \overline{\overline{Q}}_{66} \end{bmatrix} = \begin{bmatrix} \overline{Q}_{11} & \overline{Q}_{16} \\ \overline{Q}_{16} & \overline{Q}_{66} \end{bmatrix} - \begin{bmatrix} \overline{Q}_{12} & \overline{Q}_{13} \\ \overline{Q}_{26} & \overline{Q}_{36} \end{bmatrix} \begin{bmatrix} \overline{Q}_{22} & \overline{Q}_{23} \\ \overline{Q}_{23} & \overline{Q}_{33} \end{bmatrix}^{-1} \begin{bmatrix} \overline{Q}_{12} & \overline{Q}_{26} \\ \overline{Q}_{13} & \overline{Q}_{36} \end{bmatrix}.$$

The stress and strain vectors in Eq. (A.2) can be transformed to global coordinates ($x\theta r$), via the following transformation:

$$\begin{pmatrix} \sigma_x \\ \sigma_r \\ \tau_{r\theta} \\ \tau_{xr} \\ \tau_{x\theta} \end{pmatrix} = \begin{bmatrix} m^2 & 0 & 2mn & 0 \\ n^2 & 0 & -2mn & 0 \\ 0 & m & 0 & -n \\ -mn & 0 & m^2 - n^2 & 0 \\ 0 & n & 0 & m \end{bmatrix} \begin{pmatrix} \sigma_{\overline{x}} \\ \tau_{\overline{\theta z}} \\ \tau_{xz} \\ \tau_{x\theta} \end{pmatrix},$$

and

$$\begin{pmatrix} \varepsilon_x \\ \varepsilon_r \\ \gamma_{r\theta} \\ \gamma_{xr} \\ \gamma_{x\theta} \end{pmatrix} = \begin{bmatrix} m^2 & 0 & mn & 0 \\ n^2 & 0 & -mn & 0 \\ 0 & m & 0 & -n \\ -2mn & 0 & m^2 - n^2 & 0 \\ 0 & n & 0 & m \end{bmatrix} \begin{pmatrix} \varepsilon_{\overline{x}} \\ \gamma_{\overline{\theta z}} \\ \gamma_{\overline{xz}} \\ \gamma_{x\theta} \end{pmatrix}. \tag{A.3}$$

In Eq. (A.3), $m = \cos(\zeta)$ and $n = \sin(\zeta)$, where ζ is the angle between the global coordinate x and the meridian coordinate $\overline{x}$. Substituting Eq. (A.3) into Eq. (A.2) gives

$$\begin{pmatrix} \sigma_x \\ \sigma_r \\ \tau_{r\theta} \\ \tau_{xr} \\ \tau_{x\theta} \end{pmatrix} = \begin{bmatrix} \widetilde{Q}_{11} & \widetilde{Q}_{13} & \widetilde{Q}_{14} & \widetilde{Q}_{15} & \widetilde{Q}_{16} \\ \widetilde{Q}_{31} & \widetilde{Q}_{33} & \widetilde{Q}_{34} & \widetilde{Q}_{35} & \widetilde{Q}_{36} \\ \widetilde{Q}_{41} & \widetilde{Q}_{43} & \widetilde{Q}_{44} & \widetilde{Q}_{45} & \widetilde{Q}_{46} \\ \widetilde{Q}_{51} & \widetilde{Q}_{53} & \widetilde{Q}_{54} & \widetilde{Q}_{55} & \widetilde{Q}_{56} \\ \widetilde{Q}_{61} & \widetilde{Q}_{63} & \widetilde{Q}_{64} & \widetilde{Q}_{65} & \widetilde{Q}_{66} \end{bmatrix} \begin{pmatrix} \varepsilon_x \\ \varepsilon_r \\ \gamma_{r\theta} \\ \gamma_{xr} \\ \gamma_{x\theta} \end{pmatrix}, \tag{A.4}$$

where

$$[\widetilde{Q}] = \begin{bmatrix} \widetilde{Q}_{11} & \widetilde{Q}_{13} & \widetilde{Q}_{14} & \widetilde{Q}_{15} & \widetilde{Q}_{16} \\ \widetilde{Q}_{31} & \widetilde{Q}_{33} & \widetilde{Q}_{34} & \widetilde{Q}_{35} & \widetilde{Q}_{36} \\ \widetilde{Q}_{41} & \widetilde{Q}_{43} & \widetilde{Q}_{44} & \widetilde{Q}_{45} & \widetilde{Q}_{46} \\ \widetilde{Q}_{51} & \widetilde{Q}_{53} & \widetilde{Q}_{54} & \widetilde{Q}_{55} & \widetilde{Q}_{56} \\ \widetilde{Q}_{61} & \widetilde{Q}_{63} & \widetilde{Q}_{64} & \widetilde{Q}_{65} & \widetilde{Q}_{66} \end{bmatrix}$$

$$= \begin{bmatrix} m^2 & 0 & 2mn & 0 \\ n^2 & 0 & -2mn & 0 \\ 0 & m & 0 & -n \\ -mn & 0 & m^2-n^2 & 0 \\ 0 & n & 0 & m \end{bmatrix} \begin{bmatrix} \overline{\overline{Q}}_{11} & 0 & 0 & \overline{\overline{Q}}_{16} \\ 0 & \overline{Q}_{44} & \overline{Q}_{45} & 0 \\ 0 & \overline{Q}_{45} & \overline{Q}_{55} & 0 \\ \overline{\overline{Q}}_{16} & 0 & 0 & \overline{\overline{Q}}_{66} \end{bmatrix} \begin{bmatrix} m^2 & n^2 & 0 & -mn & 0 \\ 0 & 0 & m & 0 & 0 \\ 2mn & -2mn & 0 & m^2-n^2 & 0 \\ 0 & 0 & -n & 0 & m \end{bmatrix}.$$

Since we assume that $\varepsilon_r = \gamma_{r\theta} = 0$, they can be removed from the global strain vector together with the corresponding columns (the second and third) of the stiffness matrix in Eq. (A.4), resulting in the constitutive relation given in Eq. (1).

Appendix B

B.1. The stiffness and mass expressions

$$K_{PP} = \sum_{j=1}^{n} \pi(r_0^2 - r_i^2)_j \widetilde{Q}_{11}^j, \quad K_{PT} = \sum_{j=1}^{n} \frac{2\pi}{2}(r_0^3 - r_i^3)_j \widetilde{Q}_{16}^j, \quad K_{PR} = \sum_{j=1}^{n} \pi(r_0^2 - r_i^2)_j \widetilde{Q}_{15}^j,$$

$$K_{TT} = \sum_{j=1}^{n} \frac{\pi}{3}(r_0^4 - r_i^4)_j \widetilde{Q}_{66}^j, \quad K_{TR} = \sum_{j=1}^{n} \frac{2\pi}{3}(r_0^3 - r_i^3)_j \widetilde{Q}_{56}^j, \quad K_{RR} = \sum_{j=1}^{n} \pi(r_0^2 - r_i^2)_j \widetilde{Q}_{55}^j,$$

$$m = \sum_{j=1}^{n} \rho_j \pi(r_0^2 - r_i^2)_j, \quad I = \sum_{j=1}^{n} \rho_j \frac{\pi}{4}(r_0^4 - r_i^4)_j, \quad \overline{I} = 2I,$$

$$K_{MM} = \sum_{j=1}^{n} \frac{\pi}{4}(r_0^4 - r_i^4)_j \widetilde{Q}_{11}^j, \quad K_{VV} = \sum_{j=1}^{n} \frac{\pi}{2}(r_0^2 - r_i^2)_j (\widetilde{Q}_{55}^j + \widetilde{Q}_{66}^j),$$

$$K_{VA} = \sum_{j=1}^{n} \frac{\pi}{3}(r_0^3 - r_i^3)_j \widetilde{Q}_{16}^j, \quad K_{VB} = \sum_{j=1}^{n} \frac{\pi}{3}(r_0^3 - r_i^3)_j \widetilde{Q}_{15}^j,$$

$$\overline{K}_{MM} = (\lambda^2 x/2) \sum_{j=1}^{n} \pi (r_0^2 - r_i^2)_j \widetilde{Q}_{11}^j, \quad \widetilde{K}_{MM} = (\lambda^4 x^2) \sum_{j=1}^{n} \pi \ln(r_0/r_i)_j \widetilde{Q}_{11}^j,$$

$$K_{RA} = (\lambda^2 x) \sum_{j=1}^{n} \pi (r_0 - r_i)_j \widetilde{Q}_{16}^j, \quad K_{RB} = (\lambda^2 x) \sum_{j=1}^{n} \pi (r_0 - r_i)_j \widetilde{Q}_{15}^j.$$

B.2. The block mass and stiffness matrices' components of the finite element analysis

$$Mx_{ij} = Mr_{ij} = \int_0^h m(x) N_i N_j \, \mathrm{d}x,$$

$$Mp_{ij} = \int_0^h I(x) N_i N_j \, \mathrm{d}x,$$

$$MM_{ij} = \int_0^h m(x) \xi_i \xi_j \, \mathrm{d}x,$$

$$JJ_{ij} = \int_0^L I(x) \eta_i \eta_j \, \mathrm{d}x,$$

$$Kxx_{ij} = \int_0^h K_{PP}(x) N_i' N_j' \, \mathrm{d}x,$$

$$Kxr_{ij} = \int_0^h K_{PR}(x) N_i' N_j' \, \mathrm{d}x,$$

$$Kxp_{ij} = \int_0^h K_{PT}(x) N_i' N_j' \, \mathrm{d}x,$$

$$Krr_{ij} = \int_0^h K_{RR}(x) N_i' N_j' \, \mathrm{d}x,$$

$$Krp_{ij} = \int_0^h K_{TR}(x) N_i' N_j' \, \mathrm{d}x,$$

$$Kpp_{ij} = \int_0^h K_{TT}(x) N_i' N_j' \, \mathrm{d}x,$$

$$Kuu_{ij} = \int_0^h K_{VV}(x) \xi_i' \xi_j' \, \mathrm{d}x,$$

$$Kub_{ij} = \int_0^h (\xi_i' K_{VB}(x) \eta_j' + \xi_i' K_{VV}(x) \eta_j + \xi_i' K_{RB}(x) \eta_j) \, \mathrm{d}x,$$

$$Kua_{ij} = \int_0^h (\xi_i' K_{VA}(x) \eta_j' + \xi_i' K_{RA}(x) \eta_j) \, \mathrm{d}x,$$

$$Kau_{ij} = Kua_{ij}, \quad Kbu_{ij} = Kub_{ij},$$

$$Kbb_{ij} = \int_0^h (\eta_i' K_{MM}(x)\eta_j' + \{\eta_i'\eta_j + \eta_j'\eta_i\}\{K_{VB}(x) + \overline{K}_{MM}(x)\} + \eta_i\{K_{VV}(x) + \widetilde{K}_{MM}(x) + K_{RA}(x)\}\eta_j)\,\mathrm{d}x,$$

$$Kba_{ij} = \int_0^h \{\eta_i'\eta_j - \eta_j'\eta_i\}K_{VA}(x)\,\mathrm{d}x.$$

Appendix C. Fiber angle orientation

An attractive feature of the proposed hyperbolic coupling is that its hyperbolic surface can be generated from a sequence of parallel straight lines (geodesic lines). With this feature the hyperbolic coupling, together with a fibrous composite shaft, can be readily manufactured into a single unit by using a filament winding machine. By simply placing the fibers along the geodesic lines of the hyperbola, that is, along lines parallel to AB in Fig. C.1, a fibrous composite hyperbolic ply is produced.

The fiber angle orientation, θ_f, this hyperbolic ply is a function of the axial location (x) and can be computed using the analysis presented below. Let us first introduce some of the pertinent geometric parameters of the hyperbolic ply (some of these parameters are shown in Fig. C.1):

$D_{\max}$	the maximum diameter of the hyperbola,
$D_{\min}$	the minimum diameter of the hyperbola,
L_{axial}	the axial length of the hyperbolic ply (along the axis, x),
L_f	the fiber's length (AB).
α_f	the sweep angle; that is, the angle to be rotated by one of the coupling's end as the fiber AB is being laid down,
γ	the angle between the fiber AB and the axial coordinate, x.

In Fig. C.1, AB represents a single fiber (tow) that is laid down along a geodesic line of the hyperbola. In addition, the following geometric relations can be deduced from the figure:

$$\alpha_f = 2\sin^{-1}(C/D_{\max}), \quad \beta_f = (\pi - \alpha_f)/2,$$

$$\gamma = \tan^{-1}(C/L_{\text{axial}}), \quad L_f = L_{\text{axial}}/\cos(\gamma).$$

The fiber angle orientation, θ_f, can be obtained from the dot product,

$$\cos(\theta_f) = \hat{n}_f \cdot \hat{n}_s,$$

where $\hat{n}_f$ and $\hat{n}_s$ are unit vectors along the fiber direction and the meridian coordinates $\overline{x}$, respectively,

$$\hat{n}_f = \cos(\gamma)\hat{n}_x + C\cos(\beta_f)/L_f\hat{n}_r + C\sin(\beta_f)/L_f\hat{n}_\theta$$

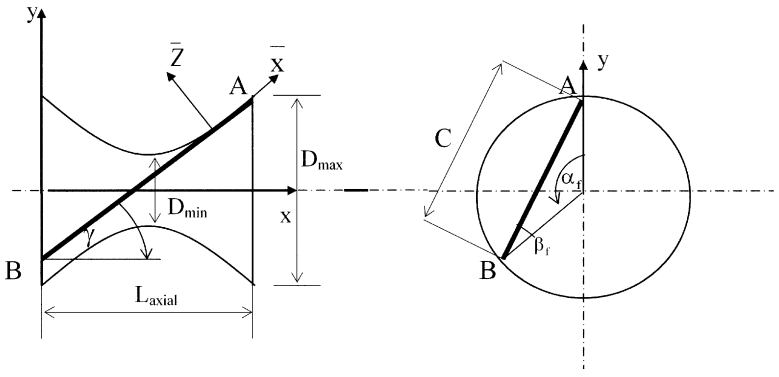

Fig. C.1. Basic geometric parameters of a hyperbolic fibrous composite ply.

and

$$\hat{n}_s = \cos(\varsigma)\hat{n}_x + \sin(\varsigma)\hat{n}_r.$$

The unit vectors $\hat{n}_x$, $\hat{n}_r$, and $\hat{n}_\theta$ are measured along the global axial coordinate, x, the radial coordinate, r, and the tangential coordinate, θ, and ζ is the angle between the meridian and axial coordinates; that is between, $\bar{x}$ and x.

The hyperbolic ply is generated by laying down the fibers in lines parallel to the geodesic line AB. In order for the coupling to efficiently carry the load when the applied torque is reversed, at least another layer of $-\theta_f$ is needed. The coupling considered in this paper is formed of two plies only, engendering a $[\pm\theta_f(x)]$ fibrous–composite–hyperbolic coupling.

Appendix D. Explanation of the jump phenomenon

To understand the jump phenomenon observed in Fig. 2, an investigation of the smallest 6 axial–radial–torsional natural frequencies of the carbon/epoxy coupling studied in the example of Fig. 2 is carried out. Based on the mathematical model developed in this paper, Eq. (6), these six natural frequencies are the first, second, and third radial (U_{r1}, U_{r2}, and U_{r3}), the first and second torsional (U_{p1}, and U_{p2}), and the first axial (U_{x1}) natural frequencies.

It should be mentioned that because of the full coupling among the axial, radial and torsional vibration, distinguishing between the different modes of vibration becomes a little ambiguous. In this paper, a specific mode of vibration (axial, radial, or torsional) is defined when the corresponding displacement pattern dominates the other two. For example, if all three displacements are experienced at a given natural frequency, and the axial displacement pattern dominates the other two, the mode shape is defined as the axial mode shape.

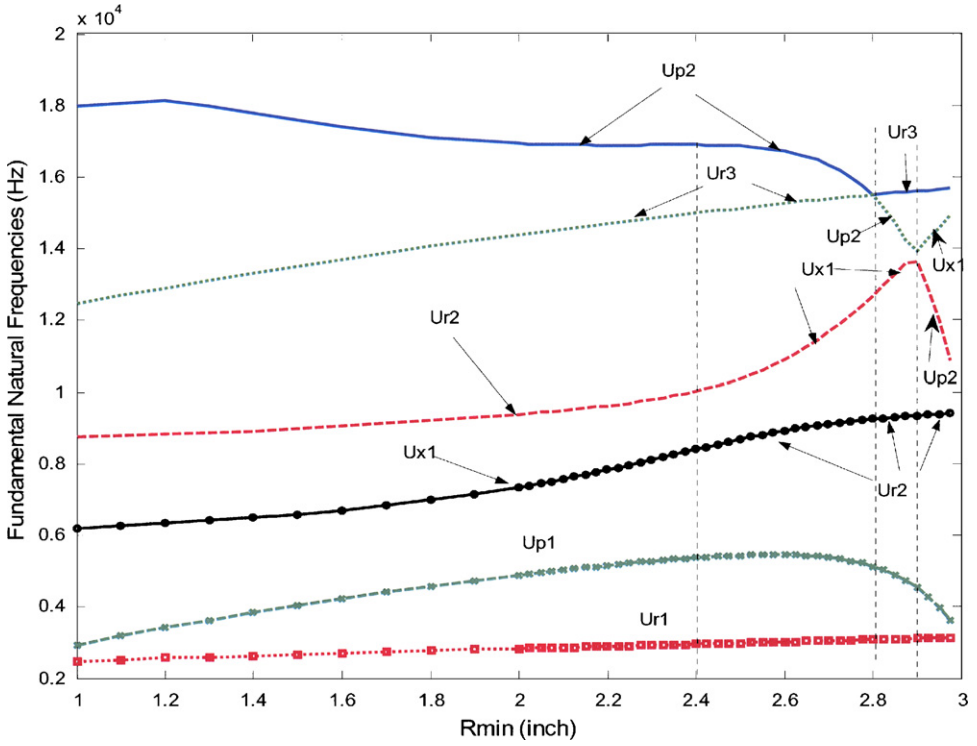

Fig. D.1. Variation of the first six natural frequencies of the coupling with $R_{\min}$. □ . . . □ . . . □ 1st natural frequency, x-.-x-.-x 2nd, o—o—o 3rd, - - - - - - - 4th, ……5th, ———6th.

Fig. D.1 displays the above-mentioned first six natural frequencies as functions of $R_{\min}$. The inserted texts in the figure indicate the mode shape associated with each frequency over a given range of $R_{\min}$. The eigenvalue curve veering phenomenon is observed three times:

1. At about $R_{\min} = 2.9$ in, the fourth and fifth natural frequencies meet and repel each other, and as they repel each other they swap their respective mode shapes ($U_{p2} \Leftrightarrow U_{x1}$).
2. At $R_{\min} = 2.8$ in, the fifth and sixth natural frequencies almost collide, repel each other, and exchange their mode shapes ($U_{p2} \Leftrightarrow U_{r3}$).
3. A much smoother curve veering occurs around $R_{\min} = 2.4$ in. As the third and fourth natural frequencies gradually approach each other, they repel each other in the vicinity of $R_{\min} = 2.4$ in and gradually depart from each other. As they depart, they also experience the mode shape swap ($U_{r2} \Leftrightarrow U_{x1}$).

It is the third curve veering (at $R_{\min} = 2.4$ in) that is responsible for the jump phenomenon observed in Fig. 2. It occurs as the first axial mode shape U_{x1}, jumps from the fourth to the third natural frequency.

References

[1] Anon, Couplings and U-joints, *Motion System Dynamics: MSD A43* 12 (2004) 1187–1192.
[2] G. Geislinger, The geislinger gesilco advanced composite coupling with high misalignment compensation capacity and low weight, *ASME Inter Combustion Engine Division* 40 (2003) 65–72.
[3] W. Jonathan, Centa's new coupling and shaft systems, *Diesel and Gas Turbine Worldwide* 37 (2005) 41.
[4] H. Ghoneim, D.J. Lawrie, Analysis of flexural vibration of a composite shaft with partial cylindrical constrained layer damping treatment, *Journal of Vibration and Control* 12 (2006) 25–55.
[5] H. Ghoneim, D.J. Lawrie, Damping of a composite driveshaft, *SPIE Proceedings, Smart Structures and Materials* 5760 (2005) 550–558.
[6] H.S. Faust, E. M. Hogan, J. Hess, Development of an integral composite drive shaft and coupling, in: *The paper presented at the National Technical Specialists' Meeting on Advanced Rotorcraft Structures*, Williamsburg, Virginia, October 1988.
[7] D.J. Lawrie, *Personal Communication*, 2004.
[8] L. Meirovitch, *Principles and Techniques of Vibration*, Prentice-Hall, Englewood Cliffs, NJ 1997, pp. 361–477.
[9] W. Kim, A. Argento, R.A. Scott, Free vibration of a rotating tapered composite Timoshenko shaft, *Journal of Sound and Vibration* 226 (1999) 125–147.
[10] J.N. Reddy, *An Introduction to the Finite Element Method*, McGraw-Hill, New York, 1993, p. 148.
[11] Z. Hashin, Complex moduli of viscoelastic composites—II: fiber reinforced materials, *International Journal of Solids and Structures* 6 (1970) 797–807.
[12] T.S. Miller, Characterization and constitutive modeling of flexible polyurethane matrix continuous-fiber composites, Technical Report 95-38, University of Delaware Center for Composite Materials, 1995.
[13] X.L. Liu, Behavior of derivatives of eigenvalues and eigenvectors in curve veering and mode localization and their relation to close eigenvalues, *Journal of Sound and Vibration* 256 (2002) 551–564.
[14] P.R. Cunningham, R.G. White, G.S. Aglietti, The effects of various design parameters on the three vibration of doubly curved composite sandwich panels, *Journal of Sound and Vibration* 230 (2000) 617–648.